

# Effect of scanning strategies on residual stress and mechanical properties of Selective Laser Melted Ti6Al4V

Haider Ali, Hassan Ghadbeigi, Kamran Mumtaz\*

Department of Mechanical Engineering, University of Sheffield, Sheffield, UK

## ARTICLE INFO

### Keywords:

Finite Element  
Cooling rate  
Selective Laser Melting  
Additive Manufacturing  
Ti6Al4V  
Residual stress

## ABSTRACT

During the Selective Laser Melting (SLM) process large temperature gradients can form, generating a mismatch in elastic deformation that can lead to high levels of residual stress within the additively manufactured metallic structure. Rapid melt pool solidification causes SLM processed Ti6Al4V to form a martensitic microstructure with a ductility generally lower than a hot working equivalent. Currently post-process heat treatments can be applied to SLM components to remove in-built residual stress and improve ductility.

This study examined the effect of scanning strategy (scan vector lengths and scan vector rotation) and re-scanning strategy on residual stress formation and mechanical properties of SLM Ti6Al4V parts. 90° alternating scanning strategy resulted in the lowest residual stress build-up for SLM Ti6Al4V parts built on both the standard and modified Renishaw platforms using a modulated Nd-YAG fiber laser. Scanning strategy did not show any direct correlation with mechanical properties. Re-scanning with 150% energy density resulted in 33.6% reduction in residual stress but the effect on mechanical properties was detrimental and samples failed prematurely. The study was based on detailed experimental analysis along with Finite Element simulation of the process using ABAQUS to understand the underlying physics of the process.

## 1. Introduction

Additive Manufacturing (AM) techniques are of interest to industry due to capability of manufacturing fully functional complex geometries from a digital model by joining material in a layer by layer manner [1,2]. Selective Laser Melting (SLM) creates high density 3D parts by selectively melting and fusing metallic powder. Cross-sections of a 3D geometry are successively fused on top of each other in a layer wise manner. SLM process provides design freedom and capability of processing high performance materials to high value markets like the aerospace industry [3]. A significant problem associated with SLM components is the development of high internal residual stress [3]. Rapid repeated heating and cooling cycles of successive layers of the powder feedstock during SLM build process is responsible for the high cooling rates and large temperature gradients associated with the process. These high cooling rates and large temperature gradients result in high residual stress build up in the SLM components. Parts can fail during an SLM build or later in service due to these high internal residual stresses [3–14]. Post processing stress relief heat treatment cycles adds up to the manufacturing time and cost of SLM components [15]. A correct understanding of the numerous physical phenomena associated with this complex fabrication process is needed in order to control

it [16]. Using incorrect process parameters for an SLM build, can lead to poor part properties (e.g. high internal porosity) and excessively high thermal stress concentration [17]. AM processes including SLM can be broken down into pre-process, in-process and post-process stages, varying parameters at each stage affects the final part properties [2,14]. Considerable research has focused on the in-process parameters and their effect on the residual stress build-up in the SLM components [3,5,6,8,11,13,18–30].

FEA simulation by Cheng et al. [22], predicted lowest residual stress and lowest deformation for IN-718 parts using 45° line scanning. Dunbar et al. [19], reported a decrease in distortion of the build and substrate when the scan pattern was rotated every layer. Another important phenomenon according to published literature is the difference in the directional stresses in SLM parts. Cheng et al. [22], reported the highest difference in directional stresses for line scanning while rotation of the scan area resulted in reducing this difference. Residual stress in the direction of the scan vector is much higher than in the transverse direction [21,22]. SLM parts or substrates deformed more along the scan direction, than the transverse direction [5,8,20]. Longitudinal stress increases with increasing scan vector length [26]. The possibilities of scanning strategies are numerous and even though most studies claim shorter scan vector lengths result in a reduction in residual stress,

\* Corresponding author.

E-mail address: [k.mumtaz@sheffield.ac.uk](mailto:k.mumtaz@sheffield.ac.uk) (K. Mumtaz).

the reason is unclear. Published literature has contradicting results for the effects of scanning strategies on residual stress. Island scanning strategy results in a reduction in residual stress [5,8,29]. Using shorter scan vectors reduced the residual stress [8,13]. According to Kruth et al. [5] and Mercelis et al. [29] Island size had no effect on residual stress. According to Lu et al. [18], IN718 SLM samples manufactured with Island scanning strategy showed residual stresses in the following sequence  $2 \times 2$  mm lowest then  $5 \times 5$  mm, then  $7 \times 7$  mm and  $3 \times 3$  mm had the highest residual stress and lowest residual stress in  $2 \times 2$  mm Island size was attributed to probable relaxation due to cracking. It can be seen that different researchers have reported different effects of Island size on residual stress and the relationship between scanning strategy and residual stress is still very unclear. Therefore this study investigated the effect of scanning strategy on residual stress and mechanical properties of SLM Ti6Al4V components.

Pre and post scanning of each layer during the SLM build process has also been reported as a means of residual stress reduction in SLM components. According to Kruth et al. [5], pre-scanning each layer with the build power and higher scan speed reduced curling angle by 8%. According to Mercelis and Kruth [29], post scanning each layer with 50% energy reduced residual stress by 30%. According to Shiomi et al. [30], residual stress reduced by 55% when each layer was re-scanned at 150% energy. From literature there is no consensus as to what the optimum re-scanning energy for residual stress reduction is or whether it is better to achieve the re-scanning energy using high power and lower exposure or lower power and higher exposure. Secondly there is no published work on the effect of re-scanning on mechanical properties. Experimental trial and error runs is the traditional route for determining the optimal process parameters and developing an understanding of the physical phenomena associated with the process. Insight from FEA simulation combined with experiments can lead to a better understanding of the process.

This is first of its kind comprehensive study on the effect of laser scanning and re-scanning strategies on residual stress build up and mechanical properties of SLM Ti6Al4V parts. This work studies the effect of scanning strategy (Scan vector length and rotation) on residual stress and mechanical properties. Secondly this work investigates the effect of re-scanning on residual stress and mechanical properties. The re-scanning energy is varied by keeping power constant and varying exposure time as well as keeping exposure constant and varying power. FEA simulation is used in combination with experimental trials to understand the underlying phenomena associated with the residual stress build up and trend in mechanical properties of SLM Ti6Al4V samples.

## 2. Experimental methodology

### 2.1. Material and processing parameters

Table 1 shows the composition of Ti6Al4V-ELI powder with a particle size of 15–45  $\mu\text{m}$  from Technik Spezialpulver (TLS), used within this investigation.

This work was carried out on the Renishaw AM250 machine using the process parameters presented in Table 2.

### 2.2. Density and microstructural testing

Using a method of area fraction analysis of representative micrographs/fields based on ASTM E2109-01 (2007) and BS 7590:1992 [31,32] the volume fraction of porosity in cube samples was

**Table 1**  
Chemical composition of Ti6Al4V-ELI powder.

Element	N	C	H	Fe	O	Al	V	Ti
% Composition	0.006	0.009	0.001	0.2	0.09	20	4.08	89.404

**Table 2**  
SLM process parameters.

Power(W)	Exposure( $\mu\text{s}$ )	Hatch Spacing ( $\mu\text{m}$ )	Point distance ( $\mu\text{m}$ )	Layer thickness ( $\mu\text{m}$ )
200	100	80	65	50

estimated. Samples were cross sectioned perpendicular to build direction, mounted and prepared for optical microscopy. Kroll's reagent (92 ml distilled water, 6 ml Nitric Acid and 3 ml Hydrofluoric Acid) was used for etching the mounted samples. Using Olympus BX60 optical microscope, images were taken at 5X to 200X magnification for microstructural analysis.

### 2.3. Mechanical properties and residual stress measurements

Three tensile test specimens were manufactured for each test case, according to ASTM- E8 / E8M-13a standard [33]. Tensile tests were performed at a crossheads displacement rate of  $0.5 \frac{\text{mm}}{\text{min}}$  using an Instron 5567B723 with clip-on extensometers based on BS EN ISO6892-1 standard [34]. Vickers hardness tests were conducted according to B EN ISO 6507-1:2005 [35] using a 5 kg load on a Zwick hardness Tester. An average hardness value was calculated for each sample using 5 indentations taken along the width of the  $30 \times 30 \times 10$  mm block cross section. For each test case three  $30 \times 30 \times 10$  mm blocks were manufactured to be used for residual stress measurement. Strain gage rosette for residual stress measurement was attached to the top surface of  $30 \times 30 \times 10$  mm SLM blocks. Residual stress was measured at a depth of 2 mm into the sample with an average error of 5–20%, using air-brasive hole drilling method based on ASTM E837-13a [36].

### 2.4. Effect of scanning strategy

The effect of scanning strategy on residual stress was determined by building three  $30 \text{ mm} \times 30 \text{ mm} \times 10 \text{ mm}$  blocks for each test case. For each test case three tensile test specimens were built for mechanical testing. Residual stress measurements, tensile testing and hardness measurement were carried out at TWI Cambridge (Table 3).

The 45° and 90° alternating strategy procedure involves turning the orientation of each over-building layer by 45° Fig. 1(a) and 90° Fig. 1(b) respectively.

Chessboard strategy involved dividing the build area into small blocks. Fig. 1(c) shows chessboard strategy with scan vectors in adjacent blocks being parallel to each other (representation of test case S-3 to S-5). Fig. 1(d) shows chessboard with scan vectors in adjacent block at 45° to each other for Test case S-6 and for each successive layer the scan vectors in each individual block were rotated by 45°. Fig. 1(e) represents Test case S-7 where scan vectors in adjacent chessboard blocks are perpendicular to each other and for each successive layer the scan vectors in each individual block were rotated by 90°. The whole scan area for all chessboard scanning cases was rotated by 90° for each successive layer.

**Table 3**  
Scanning strategy test cases.

Test Case	Scanning Strategy
S-1	45° Alternating
S-2	90° Alternating
S-3	$2 \times 2$ mm Chessboard
S-4	$3 \times 3$ mm Chessboard
S-5	$5 \times 5$ mm Chessboard
S-6	$5 \times 5$ mm Chessboard with Scan Vectors Rotated by 45° in Adjacent blocks
S-7	$5 \times 5$ mm Chessboard with Scan Vectors Rotated by 90° in Adjacent blocks

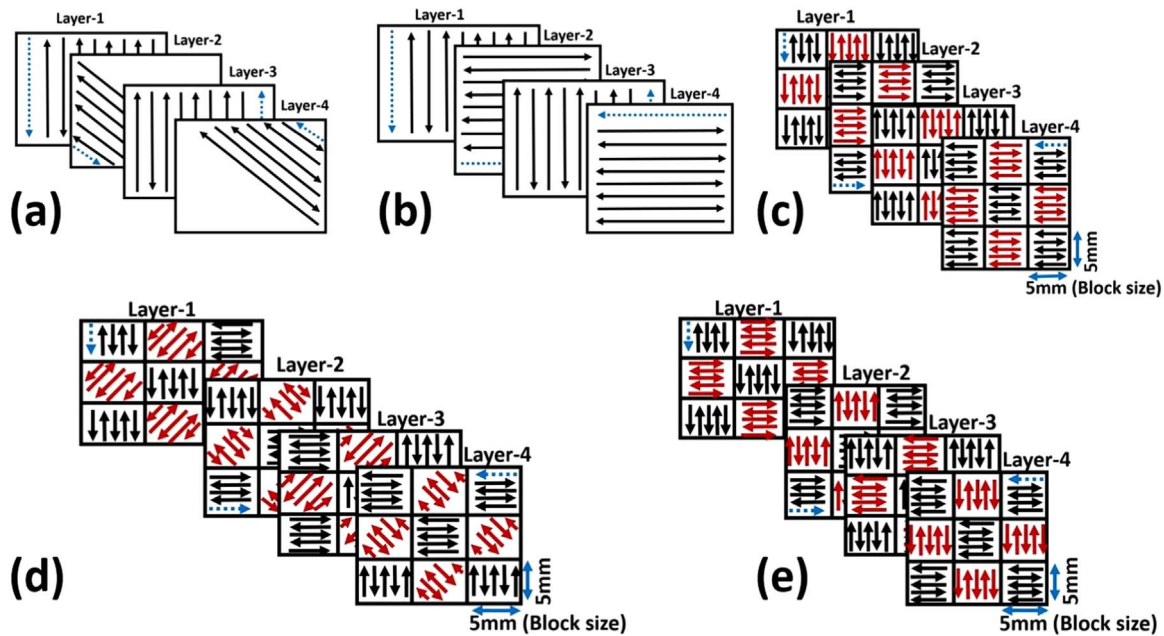


Fig. 1. Schematics of scanning strategies (a) 45° Alternating (b) 90° Alternating (c) Schematic of Chessboard Scanning (d) Chessboard Scanning with Adjacent Chessboard block Scanned in 45° rotated direction. (e) Chessboard Scanning with Adjacent Chessboard block Scanned in 90° rotated direction.

In Island scanning strategy [5,8,29], within subsequent layers the islands are shifted by 1 mm in both the X and Y directions. In this work the chessboard strategy does not shift the blocks in the subsequent layers and thus the effect of scan vector size and scan vector rotation is studied independently.

The first scan vector of each layer is shown by the blue dashed arrows. Chessboard scanning started from the blue dashed arrow, completing the scanning of all black block in the first row and then continuing on to the next row till all black blocks have been scanned. Afterwards the laser started to scan the red blocks, starting from row one and moving on to the next row till the completion of the whole layer. The same scanning order was repeated in all the following layers.

2.5. Effect of re-scanning

This set of trials involved the building of standard 30 mm × 30 mm × 10 mm test blocks and tensile specimens using the 90° build strategy and 50 μm layer thickness. After each build layer, however, the surface was re-scanned but without adding the usual layer of powder to the scan.

2.5.1. Re-scan with energy density varied by varying exposure

Re-scanning energy density was varied by keeping all other parameters constant and varying the exposure time in proportion of the optimum exposure time of 100 μs calculated from initial density optimisation trials [37]. Table 4 shows the different re-scanning trials carried out in this work, where re-scan energy density was varied by varying exposure time.

2.5.2. Re-scan with energy density varied by varying power

Re-scanning energy density was varied by keep all other parameters constant and varying the power in proportion of the optimum power of

Table 4 Re-scan with varying Exposure Test Cases.

Test case	RSE-1	RSE-2	RSE-3	RSE-4
Re-scan energy density (% of Optimum)	50	75	100	150
Re-scan exposure (μs)	50	75	100	150

Table 5 Re-scan with varying power test cases.

Test Case	RSP-1	RSP-2	RSP-3
Re-scan energy density (% of Optimum)	50	75	100
Re-scan power (W)	100	150	200

200 W calculated from initial density optimisation trials [37]. Table 5 shows the different re-scanning trials carried out in this work, where re-scan energy density was varied by varying power.

2.6. Finite element simulation

The modelling approach used within this work is based upon the concept of a moving volumetric heat source, combined with enhanced thermal conductivity. The melting behavior of a single line containing 14 laser spots was simulated. A 1.04 × 0.33 mm, powder layer of 50 μm thickness was deposited on a substrate with a thickness of 0.5 mm. A length of 1.04 mm was chosen such that only one laser spot wide extra powder is modelled at the beginning and end of laser scan track. A width of 0.325 mm was chosen such that only two laser spots wide extra powder is modelled on either side of laser scan track. The choice of small sizes for extra powder to be modelled and the small thickness of the substrate was to illustrate the effectiveness of the modelling reduction approaches. ABAQUS 8-node linear heat transfer brick elements (DC3D8) was used for meshing. A mesh size of 32.5 × 32.5 × 50 μm was used for the powder layer. The substrate mesh was biased to move from 50 μm at the top of the model, increasing to 100 μm at the bottom to minimise the number of mesh elements and reduce the computation time. The SLM process uses a localised laser beam to heat and melt feedstock from the powder bed, heat transfer therefore plays an important role in the process. The general, spatial and temporal distribution of the temperature is governed by the heat conduction equation (Eq. 1).

$$\rho C_p \frac{\partial T}{\partial t} = k_{xx} \frac{\partial^2 T}{\partial x^2} + k_{yy} \frac{\partial^2 T}{\partial y^2} + k_{zz} \frac{\partial^2 T}{\partial z^2} + \dot{q} \tag{1}$$

where T is temperature, t is time, (x, y, z) are the spatial co-ordinates, k<sub>xx</sub>, k<sub>yy</sub> and k<sub>zz</sub> are the thermal conductivities, ρ is the density, C<sub>p</sub> is the

specific heat and  $\dot{q}$  is the heat source term.

Isotropic enhanced thermal conductivity FEA model with the SLM laser modelled as a penetrating volumetric heat source and powder as a continuum was built using ABAQUS with user subroutines. Movement of laser was modelled using DFLUX subroutine, while the phase change of Ti6Al4V from powder to liquid to solid was modelled using USDFLD subroutine. Temperature dependent material properties of solid and powder Ti6Al4V used in this research were taken from the work by Roberts [13], except thermal conductivity of powder Ti6Al4V which was taken from the work by Parry et al. [26].

In order to understand the effect of scan vector length on the temperature evolution and cooling rates in the powder bed FEA simulation with varying scan vector lengths (2, 3 and 5 mm) was run to simulate six scan vectors. The powder layer was assigned powder Ti6Al4V properties and the substrate was assigned solid Ti6Al4V properties.

In order to understand the effect of varying rescanning energy density (varying power or exposure) on the temperature evolution and cooling rates in powder bed a single line FEA simulation containing fourteen laser spots was created. Substrate and powder were both assigned the properties of solid Ti6Al4V. FEA simulations were run for all the cases shown in Tables 4, 5.

### 3. Results and discussion

#### 3.1. Effect of scanning strategy

Understanding the effect of scanning strategy on SLM parts is a complex problem in itself due to the number of parameters associated with scanning strategy. Varying the size of the scan vector length, the orientation of the scan vectors, the order of scanning and the rotation of each subsequent layer can result in a significant combinations of scanning strategies. In order to understand the effect of scan vector length on the temperature of the powder bed FEA simulation with varying scan vector length was run to simulate six scan vectors. The temperature history of a point in the center of the surface of the first melt-pool was extracted from the FEA simulation. Fig. 2 shows the temperature variation of a single point on the top center of the first melt-pool. It can be seen from Fig. 2 that residual heat in already scanned region decreases with increasing scan vector length. When the laser comes back to scan a region adjacent with the already sintered material it reheats the previously solidified material. As the laser moves further from the sintered region of interest the effect of the laser on the temperature decreases.

In order to better understand the effect of scan vector length on SLM parts cooling rates were calculated for the same spot based on the reheating effect from next scan vectors. Fig. 3 shows the effect of scan vector length on the cooling rate of the top center of the first melt-pool. It can be seen from Fig. 3 that the initial cooling rate of the melt-pool is independent of the scan vector length. When the laser comes back

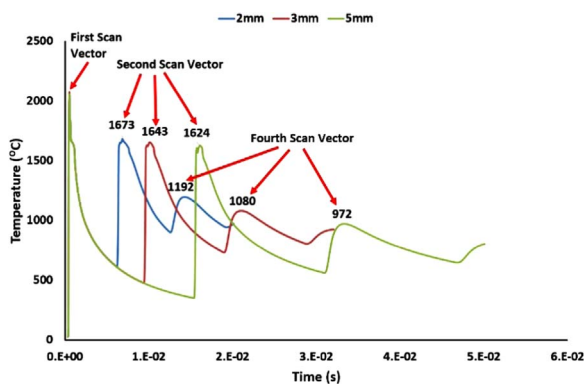


Fig. 2. Effect of scan vector length on temperature.

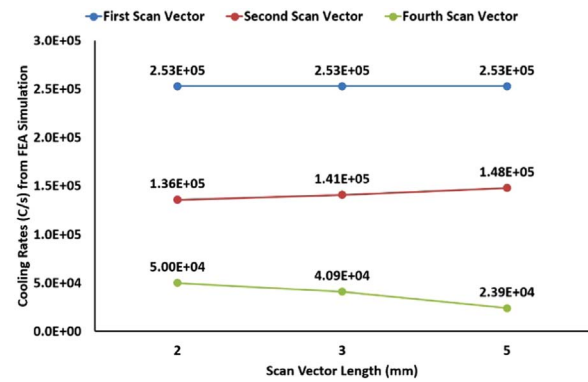


Fig. 3. Effect of scan vector length on cooling rate.

adjacent to the point of interest in the second scan vector it reheats the already sintered material as shown by the temperature history shown in Fig. 2. It can be seen that increasing the scan vector length increases the cooling rate of the reheated sintered material. The laser comes back adjacent to the point of interest in the fourth scan vector and reheats the point of interest as can be seen in Fig. 2. It can be seen from Fig. 3 that the cooling curve becomes less steep for the reheated sintered material with increasing scan vector length. Fig. 3 also shows that the sintered material reheated due to the effect of fourth scan vector adjacent to it cools slowly with increasing scan vector length. Figs. 2 and 3 show a complicated cooling behavior with varying scan vector length.

#### 3.1.1. Effect of scanning strategy on porosity and microstructure

Residual stress blocks were cross sectioned for further analysis, after residual stress measurement. Results of porosity analysis on samples created with different scanning strategies are presented in Fig. 4. Test case S-1 built with 45° alternating strategy showed 0.3% porosity while the porosity level in test case S-2 built with 90° alternating strategy was 0.1% and agreed with initial parameter optimisation trials presented in the work by Ali et al.[37]. The only factor that could be responsible for higher porosity in Test case S-1 is that 45° rotation of the successive layers resulted in the scan vectors on the sides being shorter (see Fig. 1(a)) and thus having an enhanced residual heat effect. The decreasing trend in the % porosity with increasing scan vector length for samples built with Chessboard scanning strategy (see Fig. 1(c)), can be attributed to the fact that increasing scan vector length will result in a decrease in the residual heat effect from previous scan vectors as shown in Fig. 2 and thus a decrease in the maximum temperature. Decrease in maximum temperature due to the residual heat effect of increasing scan vector length has also been reported by Cheng *et-al*[22]. Test case S-3 built with a scan vector length of 2 mm resulted in the highest residual heat effect due to shorter scan vectors and thus highest porosity of 0.9%. Increasing the scan vector length to 5 mm for test case S-5

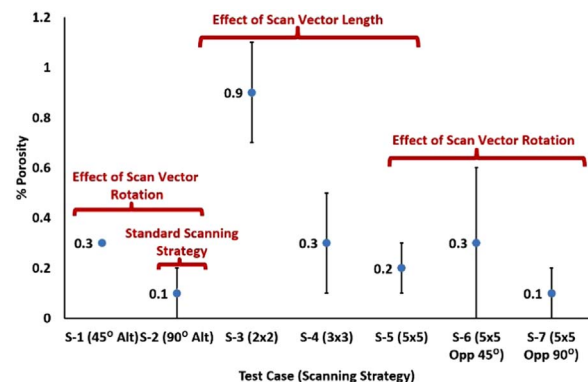


Fig. 4. Effect of scanning strategy on % porosity.

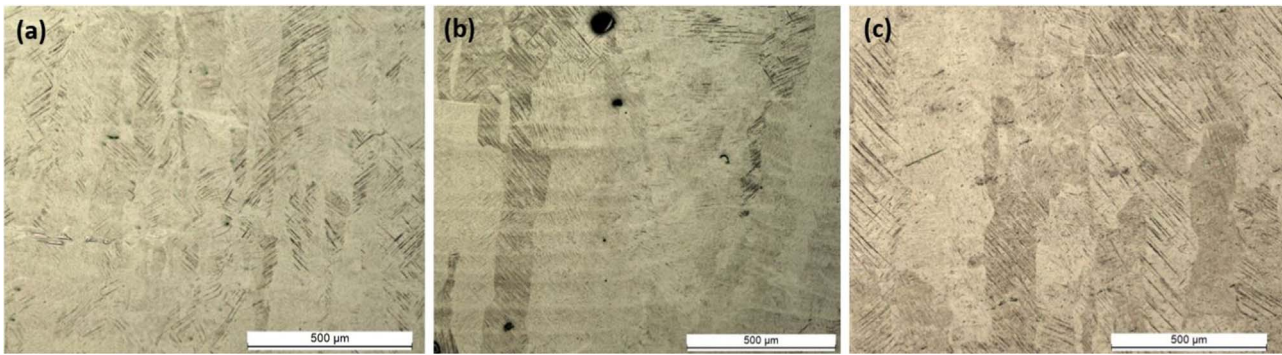


Fig. 5. Martensitic  $\alpha'$  laths in prior  $\beta$  columnar grains (a) Test case S-1,  $90^\circ$  alternating scanning strategy. (b) Test case S-3,  $3 \times 3$  Chessboard scanning strategy. (c) Test case S-5,  $5 \times 5$  Chessboard scanning strategy with scan vectors rotated at  $90^\circ$  in adjacent Chessboards.

resulted in reduced residual heat effect from the previous scan vector and thus the porosity level has decreased to 0.2%. Slight increases in porosity for Test case S-6 could be attributed to similar effects as Test case S-2. Scan vectors rotated at  $45^\circ$  in adjacent blocks resulted in some shorter vectors generated in the chessboard squares on the corners (see Fig. 1(d)). These shorter scan vectors would lead to an increased residual heat effect and thus an increase in % porosity. Decrease in % porosity to 0.1 when the scan vectors are rotated by  $90^\circ$ , in adjacent chessboard squares for test case S-7, for 5 mm scan vectors is unclear as no change in residual heat effect compared to test case S-5 would be expected. The only probable reason could either be that rotation of scan vectors in adjacent Chessboards reduces the possibility of defect stacking in successive layers. It could even be due to the stochastic nature of the SLM process.

Samples prepared for porosity analysis were etched with Kroll's etching reagent to understand the effect of scanning strategy on the microstructure. Fig. 5 shows that irrespective of the scanning strategy the samples resulted in martensitic  $\alpha'$  laths growing inside columnar prior  $\beta$  grains. Even though the cooling rates are lowered with decreasing scan vector length but they are still much higher than the cooling rate required for fully martensitic microstructure in Ti6Al4V. According to Ahmed et al. [38], cooling rates higher than  $410 \frac{C}{s}$  leads to fully martensitic microstructure for Ti6Al4V. Therefore irrespective of scanning strategy, samples from all test cases S-1 to S-7 resulted in fully martensitic microstructure with martensitic  $\alpha'$  laths growing inside columnar prior  $\beta$  grains.

### 3.1.2. Effect of scanning strategy on residual stress

Residual stress was measured on the  $30 \times 30 \times 10$  mm test blocks manufactured using different scanning strategies by means of air-brasive hole drilling and strain gauge method. Test case S-1, samples built with  $45^\circ$  Alternating strategy resulted in 110 MPa residual stress. Test case S-2, samples built with  $90^\circ$  Alternating strategy proved to be the best for achieving minimum residual stress and resulted in 107 MPa as shown in Fig. 6. Chessboard scanning strategy showed a trend of increasing Residual Stress with increasing Chessboard blocks size. Fig. 6 shows that test case S-3, with a scan vector length of 2 mm resulted in 173 MPa residual stress. Dividing the scan area into  $2 \times 2$  mm Chessboards resulted in an increase of 61.7% in residual stress, compared to test case S-2, samples built with standard  $90^\circ$  Alternating scanning strategy. Increasing the scan vector length to 3 mm, for test case S-4 resulted in a further increase of 6.9% compared to S-3% and 72.9% compared to S-2. Increasing the Chessboard size to  $5 \times 5$  for test case S-5, resulted in a residual stress of 278 MPa, which was 50.3% higher than S-4% and 159.8% higher compared to S-2. It can be seen from Fig. 6 that for Chessboard scanning strategy increasing the length of scan vector resulted in an increase in residual stress.

In order to understand the effect of scan vector rotation on residual stress using Chessboard scanning strategy, the orientation of the scan

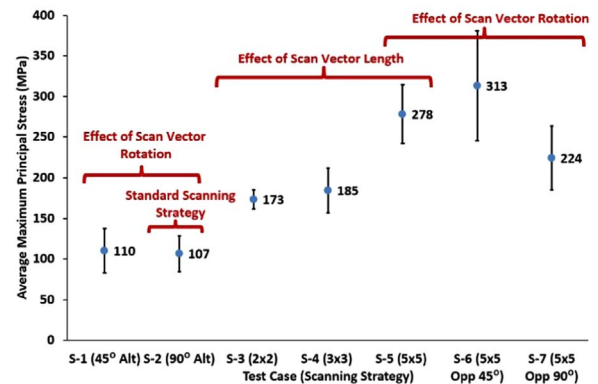


Fig. 6. Effect of scanning strategy on residual stress.

vectors in adjacent Chessboards for  $5 \times 5$  Chessboard case was rotated by  $45^\circ$  and  $90^\circ$  respectively for Test case S-6 and S-7. Fig. 6 shows that test case S-6, built with  $5 \times 5$  Chessboard scanning strategy with Scan Vectors at  $45^\circ$  in adjacent Chessboards blocks and  $90^\circ$  rotation of the whole chessboard as well as  $45^\circ$  rotation of the Scan Vectors inside the Chessboards blocks in the next layer resulted in increasing the residual stress by 12.6% compared to S-5. Fig. 6 shows that test case S-7, built with  $5 \times 5$  Chessboard scanning strategy with Scan Vectors perpendicular to each other in adjacent Chessboards blocks and  $90^\circ$  rotation of the whole chessboard as well as Scan Vectors inside the Chessboards in the next layer resulted in reducing the residual stress by 19.4% compared to S-5. The Residual Stresses in Test case S-7 samples was 209% of test case S-1, samples built with the standard  $90^\circ$  Alternating Strategy as shown in Fig. 6. Therefore  $90^\circ$  Alternating strategy was chosen to be used for the rest of this work.

The effect of scanning strategy on residual stress is complex and published literature shows varying effect of scan vector length and rotation on residual stress. The cooling rates estimated from FEA simulation shown in Fig. 3 also confirm the complexity of the relationship between scanning strategy and material behavior. Island scanning strategy has been proposed as a means of residual stress reduction in SLM components by many researchers [5,8,29]. This work used different Chessboard block sizes to see the effect of Chessboard scanning strategy on residual stress but  $90^\circ$  Alternating strategy proved to be the best for achieving minimum residual stress.

The results contradicted with the popular conception of dividing the scan area into small regions being an effective strategy for residual stress reduction in SLM parts. Therefore only  $90^\circ$  alternating and  $5 \times 5$  Chessboard scanning strategies were tested on samples created on the Renishaw SLM125 machine at The University of Sheffield. In order to make sure that enough parameters had been changed, the sample size was chosen to be  $25 \times 25 \times 10$  mm instead of the  $30 \times 30 \times 10$  mm used for samples built on the Renishaw AM250 machine at TWI, South

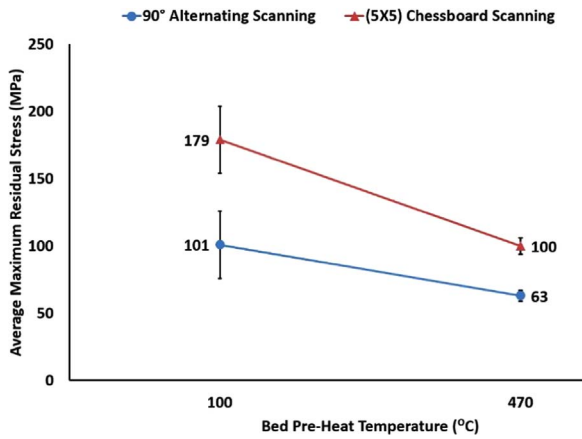


Fig. 7. Effect of scanning strategy on residual stress in 25 × 25 × 10 mm samples built at different bed pre-heat temperatures using Renishaw SLM125 machine.

Yorkshire. Instead of using the optimum combination of parameters of 200 W power and 100 μs exposure for these samples a power of 120 W and exposure of 180 μs was used. It can be seen from Fig. 2 of the work by Ali et al. [37] that this set of parameters lie at the other end of the parameter optimisation array but still resulted in 99.95% dense parts. To further clarify the effect of scanning strategy on residual stress 25 × 25 × 10 mm samples were also built at a bed pre-heat temperature of 470 °C on a custom designed heated bed used in the Renishaw SLM125 machine using 90° alternating and 5 × 5 Chessboard scanning strategies. Fig. 7 shows that samples built at 100 °C bed pre-heat temperature on the standard Renishaw SLM125 machine resulted in 179 MPa residual stress using 5 × 5 Chessboard scanning strategy while 90° alternating scanning strategy resulted in 43.6% lower residual stress in the 25 × 25 × 10 mm samples built with 120 W power and 180 μs exposure. Raising the bed temperature to 470 °C resulted in a decrease in residual stress for both scanning strategies as shown in Fig. 7. It can be seen that 5 × 5 Chessboard scanning strategy resulted in 100 MPa residual stress in the samples built at 470 °C bed pre-heat temperature while 90° alternating scanning strategy resulted in only 63 MPa residual stress in the higher temperature samples.

Even though the relationship between scanning strategy and its effect on residual stress could not be established and will require a more detailed investigation to properly understand the effect of scanning strategy on residual stress, it was established from this work that 90° alternating scanning strategy results in lower residual stress in SLM parts built on Renishaw SLM machines. Therefore for the remainder of this work 90° alternating scanning strategy was used for all samples.

### 3.1.3. Effect of scanning strategy on mechanical properties

It can be seen from Fig. 8 that the scanning vector length or rotation does not affect the yield strength of SLM Ti6Al4V samples considerably and the small variation can be attributed to the stochastic nature of the process. Chessboard scanning strategy did not show any clear trend in % elongation values with increasing Chessboard size. Fig. 8 shows that there is no clear correlation between % elongation and % porosity as well. Even though test case S-4 has lower porosity than S-3 but it also has low elongation. The porosity decrease only slightly for test case S-5 and S-7 but there is a considerable improvement in elongation. Test case S-6 and S-4 have the same level of porosity but the % elongation values are considerably different. Therefore it is not possible to establish any clear trend between porosity and elongation. Fig. 8 therefore presents no clear relationship between scanning strategy and mechanical properties.

Similarly the cooling rates for reheated sintered material from subsequent scan vectors presented in Fig. 3 also does not show any clear relationship with the elongation of the SLM Ti6Al4V samples.

Scanning strategy did not have any considerable effect on the

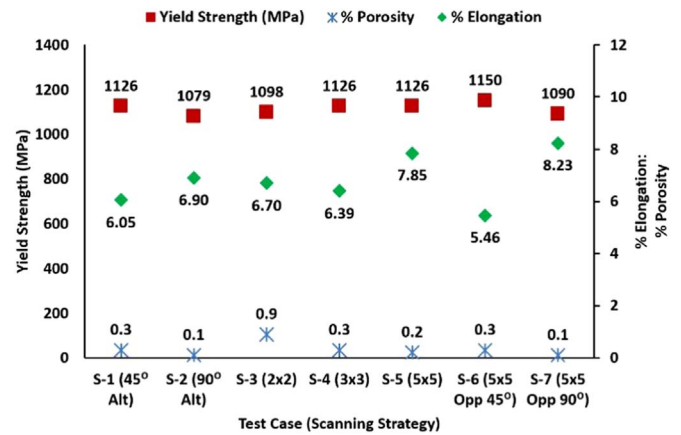


Fig. 8. Relationship between scanning strategy % porosity, % elongation and yield strength.

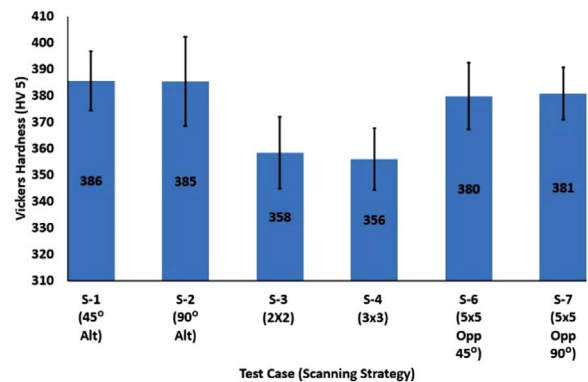


Fig. 9. Effect of scanning strategy on Vickers Hardness.

Vickers hardness of the samples as shown in Fig. 9, as the samples held similar martensitic microstructure. The slightly lower values of test case S-3 and S-4 may be a result of higher porosity levels. Yet again the porosity level in Test case S-6 is the same as Test case S-4 but the hardness values differ considerably and therefore establishing a clear link of hardness with porosity is not possible. The variation could possibly be due to measurement errors or the variation of indentation location on the samples for Vickers hardness.

### 3.2. Effect of re-scanning varying exposure

In order to understand the effect of re-scanning with varying exposure on residual stress and mechanical properties, FEA simulation with different re-scanning exposure was used to estimate the effect of re-scanning with varying exposure on cooling rates. Energy Density for re-scanning each layer was varied by keeping power constant at 200 W and varying the exposure time in proportion to the optimum exposure time of 100 μs (from density optimisation trials presented in the work by Ali et al. [37]).

Fig. 10 shows a direct relation between re-scanning exposure and melt-pool size of the re-melted material (red color denotes re-melted material, blue denotes the material unaffected by laser energy while orange to green denotes the heat affected zone). Increasing the re-scanning exposure resulted in a larger re-melted melt-pool. Larger melt-pools result in a larger volume of material to cool and thus a reduced cooling rate. An important feature to note from the FEA results in Fig. 10 is that for test case RSE-1, using 50 μs exposure for re-scanning shown in Fig. 10(a), the size of the re-melted melt-pool is relatively small. With 50 μs the FEA predicted isolated re-melted spots (i.e did not produce a continuous re-melted line).

Fig. 11 shows that there is an inverse relationship between re-

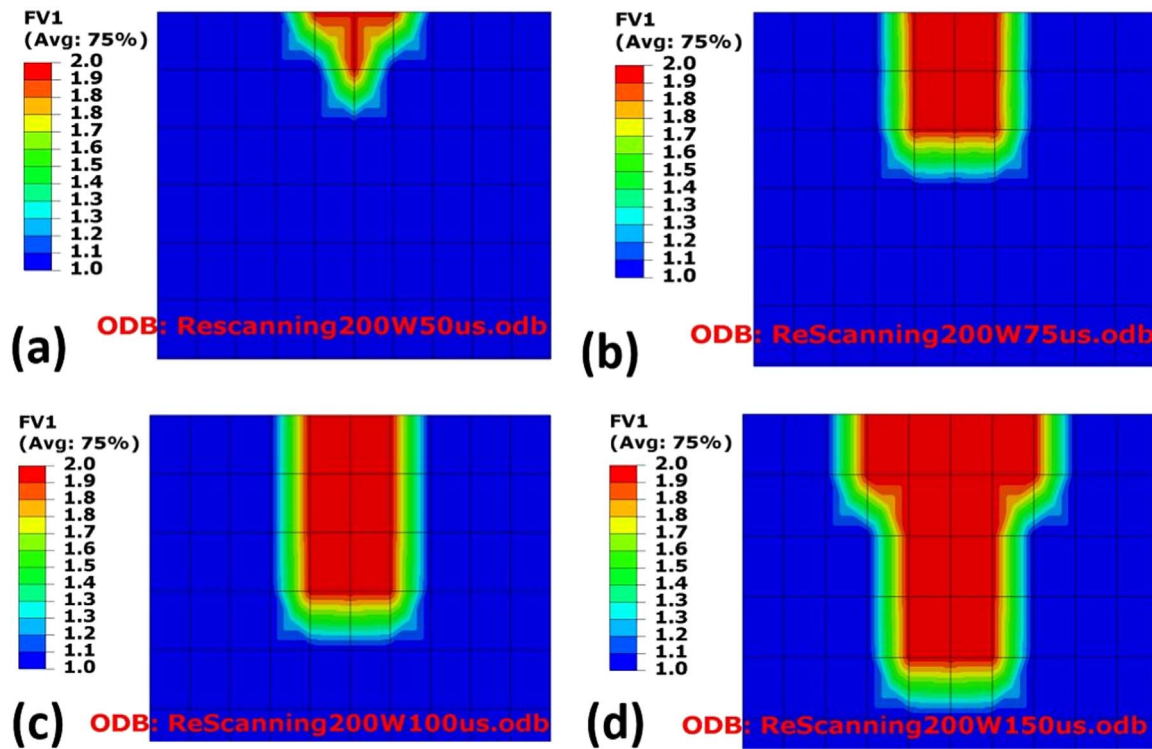


Fig. 10. Effect of re-scanning with varying exposure on melt-pool dimensions (a) Test Case RSE-1 (50  $\mu$ s Exposure), (b) Test Case RSE-2 (75  $\mu$ s Exposure), (c) Test Case RSE-3 (100  $\mu$ s Exposure) and (d) Test Case RSE-4 (150  $\mu$ s Exposure).

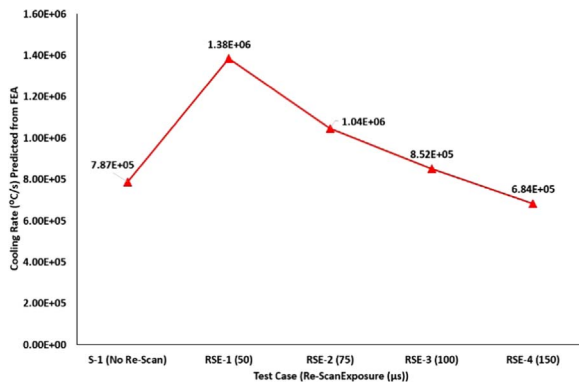


Fig. 11. Effect of re-scanning with varying exposure on cooling rates.

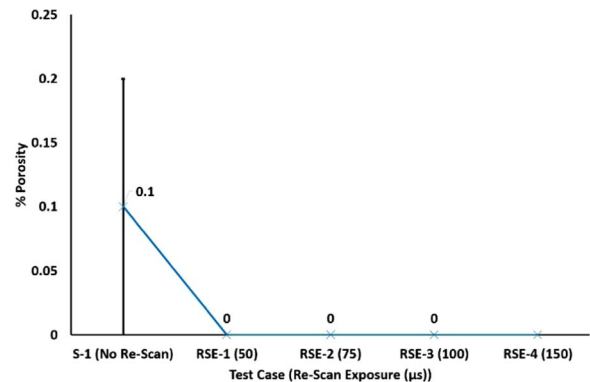


Fig. 12. Effect of re-scanning with varying exposure on % porosity.

scanning exposure and cooling rates for re-melted material. Increasing re-scanning exposure results in lowering the cooling rates. Another important feature worth noting from Fig. 11 is that the only re-scanning case resulted in a cooling rate lower than test case S-1, samples built without re-scanning is test case RSE-4, with a re-scanning exposure time of 150  $\mu$ s (Re-scanning Energy Density is 150% of the Energy Density used for melting each layer). The trends in cooling rate agree with the amount of re-melted material.

### 3.2.1. Effect of re-scanning with varying exposure on porosity and microstructure

For all the re-scanning test cases with varying exposure resulted in nearly fully dense SLM Ti6Al4V parts as shown in Fig. 12. Fig. 10 showed that increasing the re-scanning exposure resulted in an increase in the re-melted melt-pool dimensions, but porosity analysis on the experimental samples did not show any variation in the density of the samples.

Getting nearly fully dense SLM parts with re-scanning is consistent with the findings of Yasa et al. [39], reporting a reduction in porosity of

SLM parts from 0.77% to 0.032% with re-melting. Fig. 11 shows that for rescanning with varying exposure, increasing the rescanning exposure leads to reduced cooling rates. Even though the cooling rates are lowered with increasing exposure but are still much higher than the cooling rate required for fully martensitic microstructure in Ti6Al4V. According to Ahmed et al.[38], cooling rates higher than  $410 \frac{^{\circ}\text{C}}{\text{s}}$  leads to fully martensitic microstructure for Ti6Al4V. Therefore irrespective of the rescanning exposure, samples from all test cases RSE-1, RSE-2, RSE-3 and RSE-4 resulted in fully martensitic microstructure with martensitic  $\alpha'$  laths growing inside columnar prior  $\beta$  grains. Porosity analysis showed nearly fully dense samples for all the test cases of rescanning with varying exposure but a careful examination of the microstructural images revealed that there was a considerable amount of micro porosity in the samples not picked up in porosity analysis. The reason for not observing micro porosity in polished samples is because of the smearing effect as reported by Kasperovich et al.[40].

Fig. 13 shows that the amount of micro porosity in test case RSE-1, samples built with rescanning exposure of 50  $\mu$ s is higher than test case S-1, samples built without rescanning. Increasing the rescanning

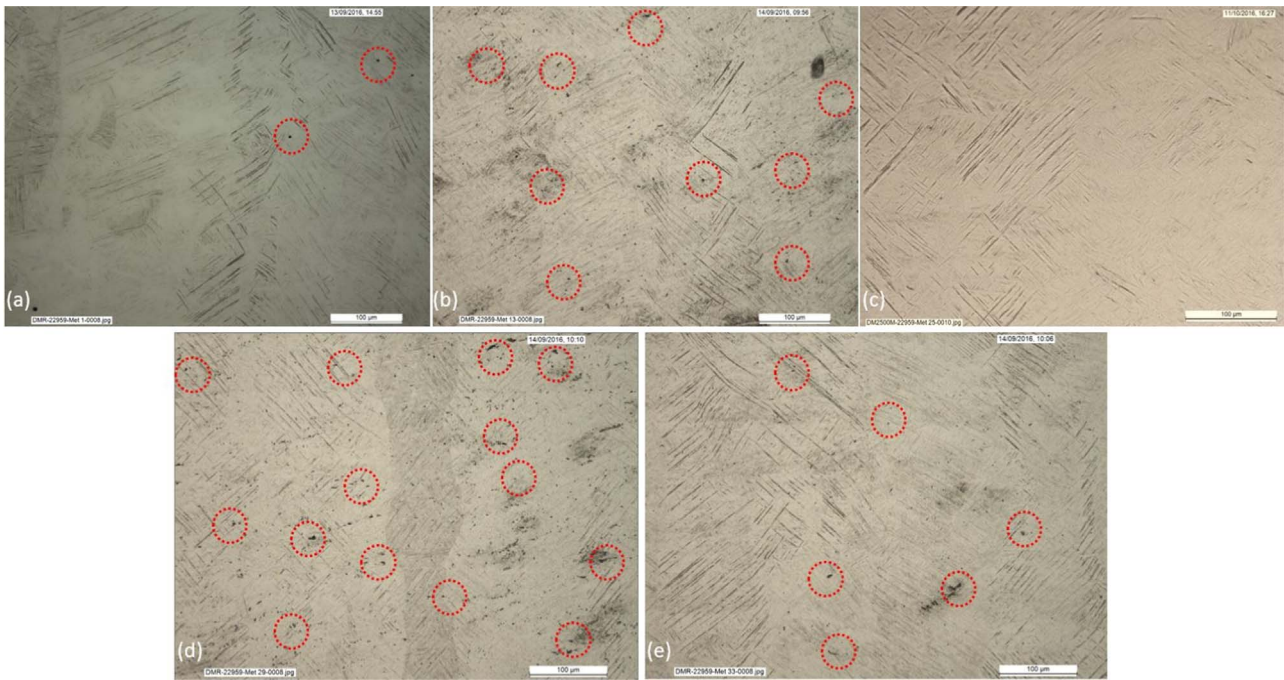


Fig. 13. Effect of re-scanning with varying exposure on micro porosity (a) Test Case S-1 (No re-scanning) (b) Test Case RSE-1 (50 μs Exposure), (c) Test Case RSE-2 (75 μs Exposure), (d) Test Case RSE-3 (100 μs Exposure) and (e) Test Case RSE-4 (150 μs Exposure).

exposure to 75 μs for test case RSE-2 the micro porosity disappeared. Test case RSE-3, built with 100 μs rescanning exposure shown in Fig. 13(d), shows the highest amount of micro porosity. Test case RSE-4 shows some micro porosity as well. Therefore in order to better understand the amount of porosity in samples, either porosity analysis need to be performed on etched samples like the work by Kasperovich et al. [40] or use more detailed analysis techniques such as micro CT.

3.2.2. Effect of re-scanning with varying exposure on residual stress

Fig. 14 shows that increasing rescanning exposure results in increasing the peak temperature in the melt-pool. For test case RSE-1 every layer was rescanned with 200 W power and 50 μs exposure, resulting in rescanning Energy Density of  $38.46 \frac{J}{mm^3}$ . Test case RSE-2 was rescanned with 200 W power and 75 μs exposure, resulting in rescanning Energy Density of  $57.69 \frac{J}{mm^3}$ . Test case RSE-3 was rescanned with 200 W power and 100 μs exposure, resulting in an Energy Density of  $76.92 \frac{J}{mm^3}$ .

For test case RSE-4 each layer was rescanned with 200 W power and 150 μs exposure, resulting in rescanning Energy Density of  $115.38 \frac{J}{mm^3}$ . This leads to higher peak temperatures as shown in Fig. 14 and larger

re-melted melt-pool size as shown in Fig. 10. It can be seen from Fig. 14 that irrespective of the rescanning Energy Density a temperature gradient exists, between the top and 250 μm depth across the re-melted melt-pool. Thus according to the temperature gradient mechanism [41] and cool down phase model [30,41], irrespective of the rescanning Energy Density, residual stress will be generated in the SLM samples.

Residual stress shows an increasing trend with rescanning exposure up to a point of 75 μs rescanning exposure and starts decreasing with further increase in rescanning exposure. According to Mercelis et al. [29], rescanning with 50% Energy Density resulted in 30% reduction in residual stress. Fig. 15 shows that rescanning with 50% Energy Density leads to an increase in cooling rates and this increase in cooling rates is responsible for the increase in residual stress of samples manufactured with re-scanning each layer with 50% Energy. The cooling rates trend seems to be agreeing well with all the cases of rescanning with varying exposure except rescanning with 50 μs exposure. This probably is a consequence of not considering the effect of the first scan on the temperature of the solidified powdered layer. Thus the FEA simulation needs further refinement for correctly predicting the cooling rates for re-melting in SLM samples. Fig. 15 shows that the only re-scanned

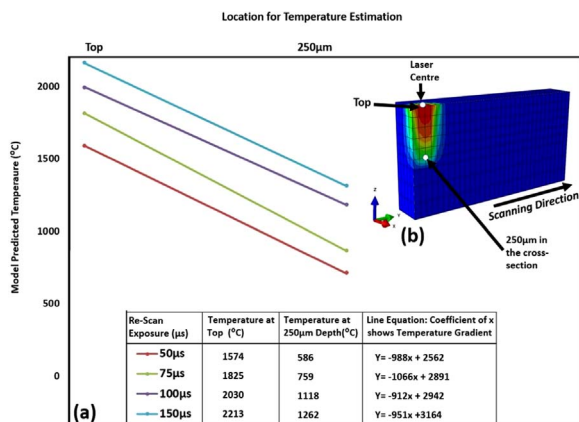


Fig. 14. Effect of rescanning with varying exposure on temperature gradient.

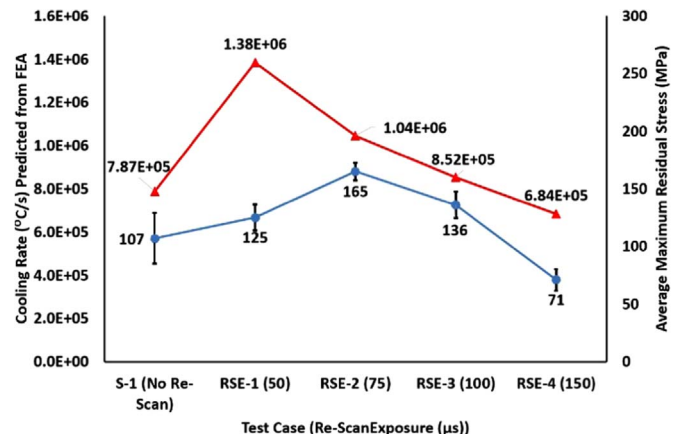


Fig. 15. Effect of re-scanning with varying exposure on cooling rate and residual stress.



samples resulting in residual stress lower than samples without re-scanning were the ones rescanned with 150  $\mu\text{s}$  re-scanning exposure. Re-scanning with 150% Energy Density for test case RSE-4 resulted in 33.6% reduction in residual stress compared with test case S-1, samples made without re-scanning. This finding agrees with findings of Shiomi et al. [30], reporting a 55% reduction in residual stress when rescanned with 150% Energy Density. The cooling rate curve in Fig. 15 also shows a decrease in cooling rate for test case RSE-4 compared with S-1 and thus the decrease in residual stress when rescanning with 150% Energy.

### 3.2.3. Effect of re-scanning with varying exposure on mechanical properties

Fig. 15 does not show any clear trend in yield strength for test cases RSE-1 to RSE-3 compared with the standard test case S-1 without any rescan. Test case RSE-4, rescanning with 150  $\mu\text{s}$  exposure showed 0.03 MPa yield strength, suggesting pre-mature failure of the tensile samples. According to Vaithilingam et al. [42], skin re-melting of SLM Ti6Al4V parts resulted in an oxide layer manufactured on Renishaw AM250 SLM machine with oxygen content in the chamber set at 50 ppm. Vaithilingam et al. [42] also reports the oxide layer being thicker on samples with skin re-melting compared to samples without re-melting. This increase in thickness of oxide layer is being attributed to the fact that melting the surface twice increased the possibility of build atmosphere oxygen penetration further into the surface. Based on the possibility of increases in the oxygen penetration further into the surface, it is hereby proposed that increases in re-melted melt-pool size has a direct relation with the oxide layer thickness. Thus the melt-pool size comparison from Fig. 10, suggests that rescanning with 150  $\mu\text{s}$  exposure would result in thicker oxide layer formation between the layers of the samples. Therefore it is valid to assume that it is these thick oxide layers resulting in the premature failure of tensile samples for test case RSE-4 and thus no measured yield strength values.

% Elongation results in Fig. 16 show a complex behavior with varying rescanning exposure. Test case RSE-1, resulted in 5.7% decrease in % elongation compared to the standard samples, test case S-1 built without rescanning. This slight decrease in elongation can be attributed to the fact that rescanning with 50  $\mu\text{s}$  exposure resulted in an increase in the micro porosity of the samples (as shown in Fig. 13(b)) as Leuders et al. [43] reports a deterioration of mechanical properties with porosity. Test case RSE-2, showed 42.5% improvement in elongation, compared to test case S-1. According to Simonelli et al. [44] rescanning each layer resulted in the transformation of  $\alpha'$  martensite into  $\alpha + \beta$  microstructure. Therefore it is valid to propose here that this 42.5% increase in elongation of test case RSE-2 samples is probably a consequence of martensite transformation into  $\alpha + \beta$ . Another factor responsible for this increase in elongation is probably the disappearance of micro porosity in test case RSE-2 samples (as shown in Fig. 13(c)).

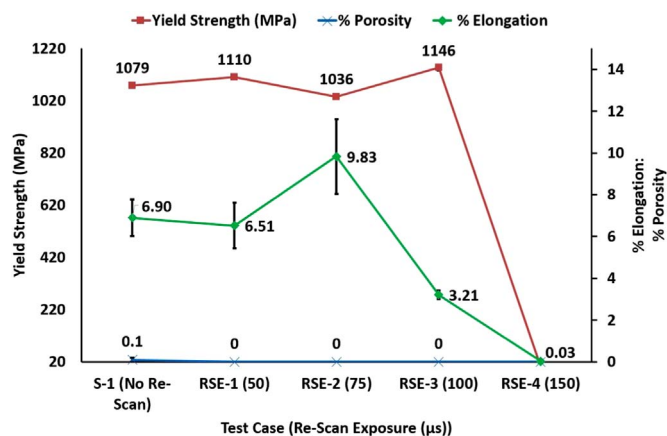


Fig. 16. Effect of re-scanning energy varying exposure on % porosity, % elongation and yield strength.

Increasing the re-scan exposure to 100  $\mu\text{s}$ , test case RSE-3 resulted in a sharp drop 53.5% in elongation compared to S-1. Fig. 13(d) shows some micro porosity in test case RSE-3 samples but this alone does not account for such a sharp decline in elongation. Another probable reason for this decrease in elongation of test case RSE-3 samples could be the increase in the oxide layer thickness between Ti6Al4V layers due to re-melting of each layer as Vaithilingam et al. [42] reported the formation of oxide layers with re-melting. Increasing the exposure to 150  $\mu\text{s}$ , test case RSE-4, resulted in 0% elongation, which suggesting pre-mature failure of the tensile samples. Based on the possibility of increase in the oxygen penetration further into the surface with re-melting [42], it is hereby proposed that increase in re-melted melt-pool size has a direct relation with the oxide layer thickness. Thus the melt-pool size comparison from Fig. 10, suggests that rescanning with 150  $\mu\text{s}$  exposure would result in thicker oxide layer formation between the layers of the samples. Therefore it is valid to assume that it is these thick oxide layers resulting in the premature failure of tensile samples for test case RSE-4 and thus no measured elongation.

Fig. 11 showed that increasing rescanning exposure led to a decrease in cooling rate but the cooling rates are still much higher than 410  $\frac{^{\circ}\text{C}}{\text{s}}$ , cooling rate leading totally martensitic microstructure for Ti6Al4V [38]. Since all the test cases RSE-1, RSE-2, RSE-3 and RSE-4 had a totally martensitic microstructure so therefore there is no major variation in Vickers hardness values for samples manufactured with different layer thicknesses (see Fig. 17). The slight decrease in the Vickers hardness of test case RSE-2 could probably be a result of possible  $\alpha'$  transformation into  $\alpha + \beta$  due to re-melting as reported by Simonelli et al. [44].

### 3.3. Effect of re-scanning with varying power

In order to understand the effect of re-scanning with varying power on residual stress and mechanical properties, FEA simulation with different re-scanning powers was used to estimate the effect of re-scanning with varying power on cooling rates. Energy Density for re-scanning each layer was varied by keeping exposure constant at 100  $\mu\text{s}$  and varying power in proportion to the optimum power of 200 W (from density optimisation trials reported in the work by Ali et al. [37]).

Fig. 18 shows a direct relation between re-scanning power and melt-pool size of the re-melted material. Increasing the re-scanning power resulted in larger re-melted melt-pool. Larger melt-pool result in more material needing to cool and thus a reduced cooling rate. An important feature to note from the FEA results in Fig. 18 is that for test case RSP-1, using 100 W power for re-scanning shown in Fig. 18(a), the FEA simulation predicted no re-melting.

Fig. 19 shows that there is the relationship between re-scanning power and cooling rate for re-melted material is not very clear. Increasing re-scanning power results in lowering the cooling rate but with 200 W power for test case RSP-3 there is a slight increase in cooling

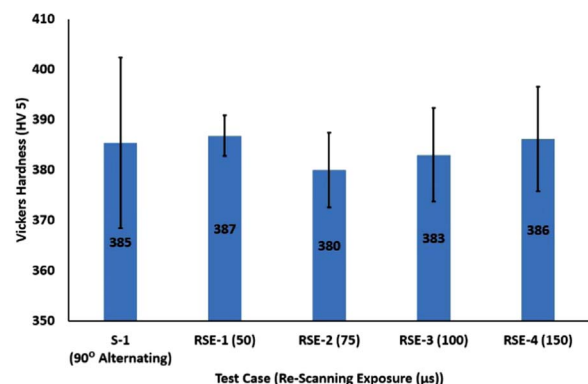


Fig. 17. Effect of re-scanning energy varying exposure on Vickers Hardness.

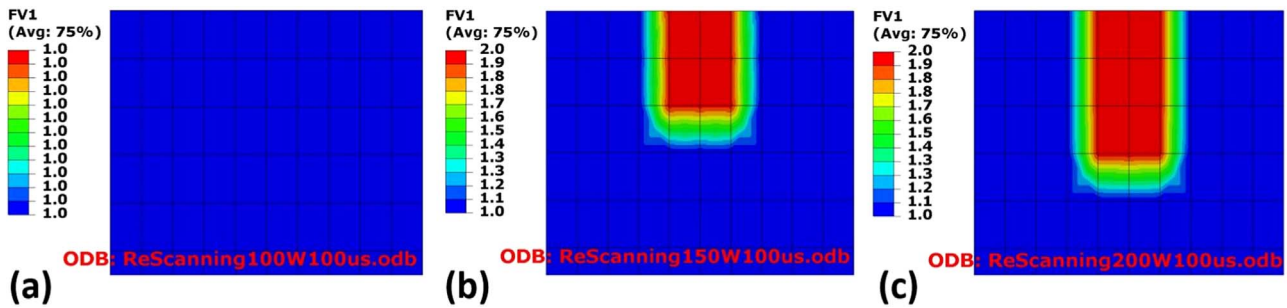


Fig. 18. Effect of re-scanning with varying power on melt-pool dimensions (a) Test Case RSP-1 (100 W Power), (b) Test Case RSP-2 (150 W Power), and (c) Test Case RSP-3 (200 W Power).

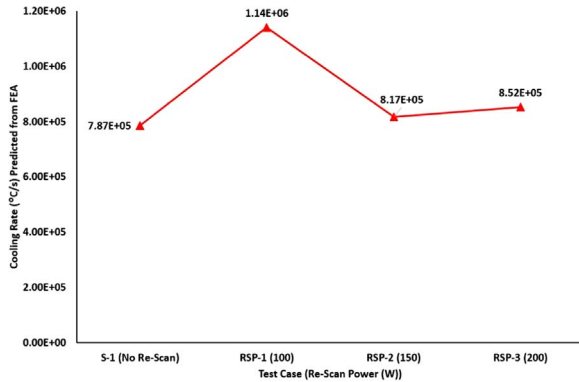


Fig. 19. Effect of re-scanning with varying power on cooling rates.

rate. Another important feature worth noting from Fig. 19 is that none of the re-scanning cases results in a cooling rate lower than test case S-1, samples built without rescanning.

### 3.3.1. Effect of re-scanning with Varying Power on Porosity and Microstructure

Re-scanning each layer of the SLM Ti6Al4V parts with varying power did not result in nearly fully dense parts, even though Yasa et al. [39] reported re-scanning as a means for improving part density. Fig. 20 shows that rescanning with lower powers resulted in an unexpected increase in porosity.

According to Fig. 21 the amount of minimum energy required for achieving nearly fully dense SLM Ti6Al4V parts from powder is inversely proportional to power.

Re-melting the solidified layers should thus require even higher energy input. Test case RSP-1 uses 100 W power, while the exposure is fixed at 100 μs (optimum exposure from Density Optimisation Trials presented in the work by Ali et al. [37]) for re-melting each layer and thus according to the results of Fig. 21 the energy input is well below

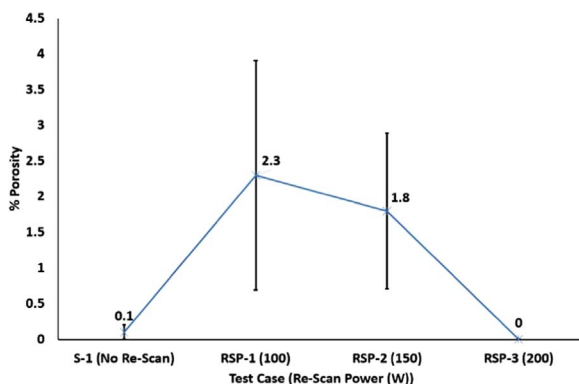


Fig. 20. Effect of re-scanning with varying power on % porosity.

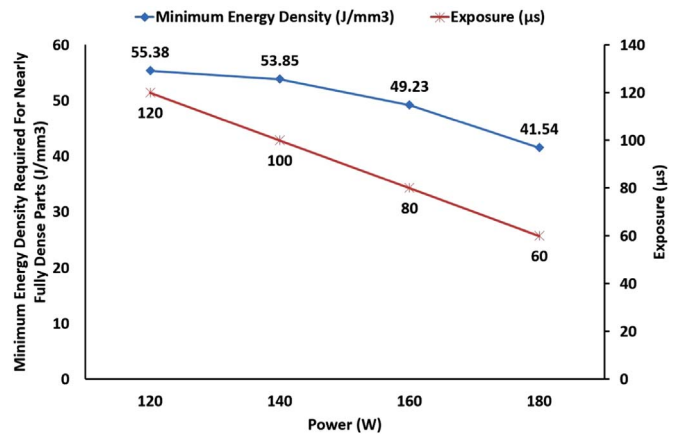


Fig. 21. Effect of power on minimum energy density required for nearly full dense Ti6Al4V SLM parts.

the requirement for nearly fully dense parts. This probably results in test case RSP-1 having 2.4% porosity. Test case RSP-2 uses 150 W power for rescanning each layer with 100 μs exposure and thus according to the trend in Fig. 21 the energy input is probably well below that required for achieving a stable re-melted melt-pool and thus results in 1.8% porosity in samples.

Fig. 19 shows that for rescanning with varying power, increasing the rescanning power leads to reduced cooling rates with a slight increase in cooling rate for test case RSP-3. Even though the cooling rates are lowered with increasing power but they are still much higher than the cooling rate required for fully martensitic microstructure in Ti6Al4V.

According to Ahmed et al. [38], cooling rates higher than  $410 \frac{^{\circ}\text{C}}{\text{s}}$  leads to fully martensitic microstructure for Ti6Al4V. Therefore irrespective of the rescanning power samples from all test cases RSP-1, RSP-2 and RSP-3 resulted in fully martensitic microstructure with martensitic α' laths growing inside prior columnar β grains as shown in Fig. 22.

### 3.3.2. Effect of re-scanning with varying exposure on residual stress

Fig. 23 shows that increasing rescanning power results in increasing the peak temperature in the melt-pool. For test case RSP-1 every layer was rescanned with 100 W power and 100 μs exposure, resulting in rescanning Energy Density of  $38.46 \frac{\text{J}}{\text{mm}^3}$ . Test case RSP-2 was rescanned with 150 W power and 100 μs exposure, resulting in rescanning Energy Density of  $57.69 \frac{\text{J}}{\text{mm}^3}$ . Test case RSP-3 was rescanned with 200 W power and 100 μs exposure, resulting in an Energy Density of  $76.92 \frac{\text{J}}{\text{mm}^3}$ . This increase in rescanning Energy Density leads to higher peak temperatures as shown in Fig. 23 and larger re-melted melt-pool size as shown in Fig. 18. It can be seen from Fig. 23 that irrespective of the rescanning Energy Density a temperature gradient exists, between the top and 150 μm depth across the re-melted melt-pool. Thus according to the temperature gradient mechanism [41] and cool down phase model [30,41], irrespective of the rescanning Energy Density with

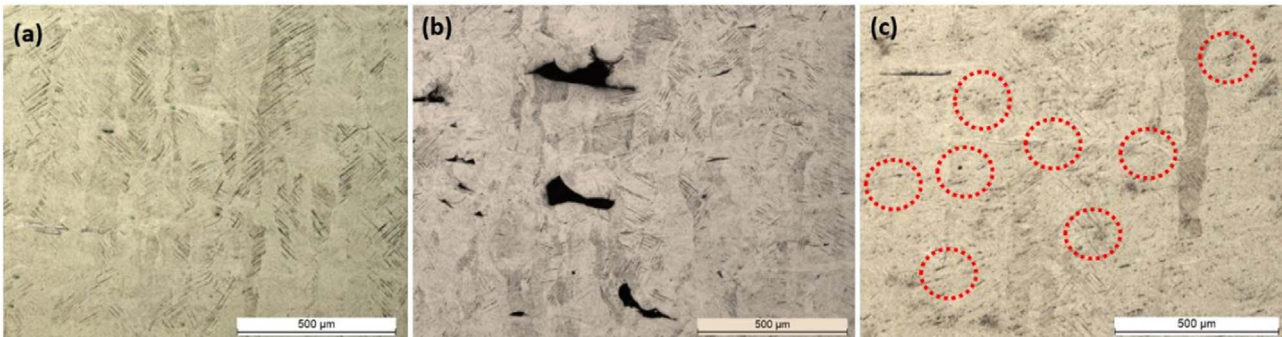


Fig. 22. Martensitic  $\alpha'$  laths in prior  $\beta$  columnar grains (a) Test case S-1, 90° alternating scanning strategy with no re-scan. (b) Test case RSP-1, re-scan with 100 W. (c) Test case RSP-3, re-scan with 200 W.

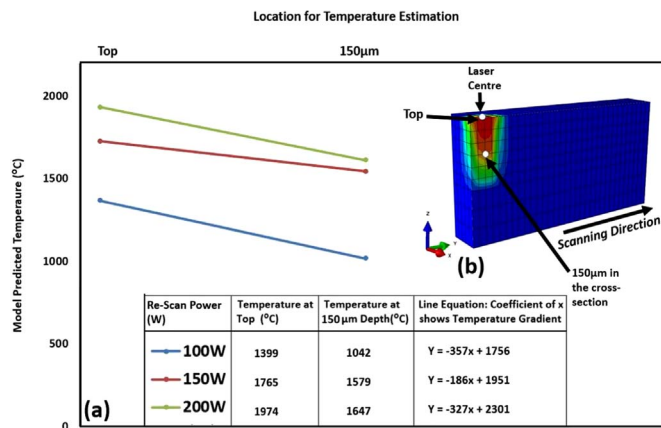


Fig. 23. Effect of rescanning with varying power on temperature gradient.

varying power, residual stress will be generated in the SLM samples.

Residual stress does not show a clear trend with rescanning power. According to Mercelis et al.[29], rescanning with 50% Energy Density resulted in 30% reduction in residual stress. Fig. 24 shows that rescanning with 50% Energy Density using 100 W power and 100  $\mu$ s exposure leads to an increase in cooling rates and this increase in cooling rates is responsible for the increase in residual stress. The cooling rates trend seems to be agreeing well with all the cases of rescanning with varying power. Fig. 24 shows that none of the rescanned samples with varying power resulted in residual stress lower than samples without rescanning.

### 3.3.3. Effect of re-scanning with varying power on mechanical properties

Fig. 25 does not show any clear trend in yield strength for test cases

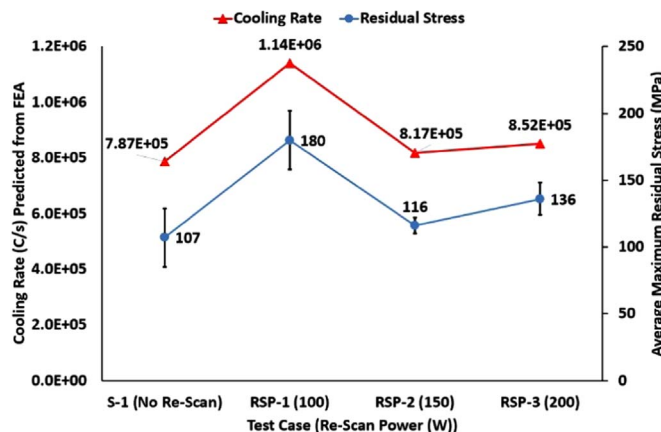


Fig. 24. Effect of rescanning with varying power on cooling rate and residual stress.

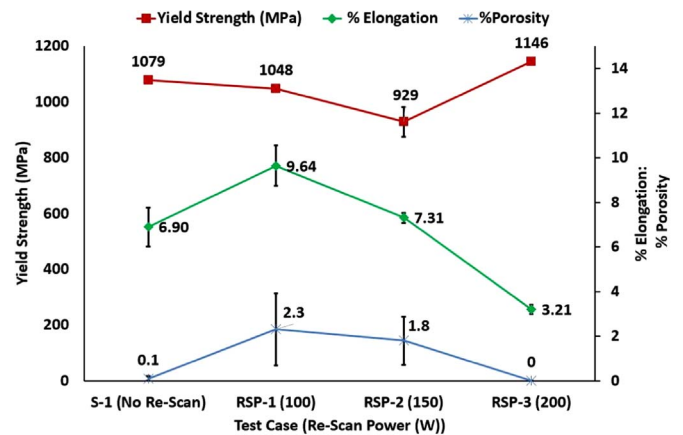


Fig. 25. Effect of re-scanning energy varying exposure on % porosity, % elongation and yield strength.

RSP-1 to RSP-3 compared with the standard test case S-1 without any rescan. Test case RSP-2, rescanning with 150 W showed 13.9% reduction in yield strength compared to test case S-1. According to Vaithilingam et al. [42], skin re-melting of SLM Ti6Al4V parts resulted in an oxide layer manufactured on Renishaw AM250 SLM machine with oxygen content in the chamber set at 50 ppm. Vaithilingam et al. [42] also reports the oxide layer being thicker on samples with skin re-melting compared to samples without re-melting. This increase in thickness of oxide layer is being attributed to the fact that melting the surface twice increased the possibility of build atmosphere oxygen penetration further into the surface. Based on the possibility of increase in the oxygen penetration further into the surface, it is hereby proposed that increase in re-melted melt-pool size has a direct relation with the oxide layer thickness. Thus the melt-pool size comparison from Fig. 18, suggests that rescanning with 150 W exposure would result in thicker oxide layer formation between the layers of the samples. Therefore it is valid to assume that it is these thick oxide layers combined with 1.8% porosity resulting in the premature failure of tensile samples for test case RSP-2 resulting in 13.9% decrease in the yield strength values. Test case RSP-3 showed an increase of 23.4% compared with RSP-2% and 6.2% compared with S-1. This increase in yield strength could probably be due to the decrease in porosity in Test case RSP-3 samples.

% Elongation results in Fig. 25 show a complex behavior with varying rescanning power. Test case RSP-1, resulted in 39.7% increase in % elongation compared to the standard samples, test case S-1 built without rescanning. According to Simonelli et al.[44], rescanning each layer resulted in the transformation of  $\alpha'$  martensite into  $\alpha + \beta$  microstructure. Therefore it is valid to propose here that this 39.7% increase in elongation for test case RSP-1 samples is probably a consequence of martensite transformation into  $\alpha + \beta$ . Test case RSP-2, rescanning each layer with 150 W resulted in 24.17% decrease in

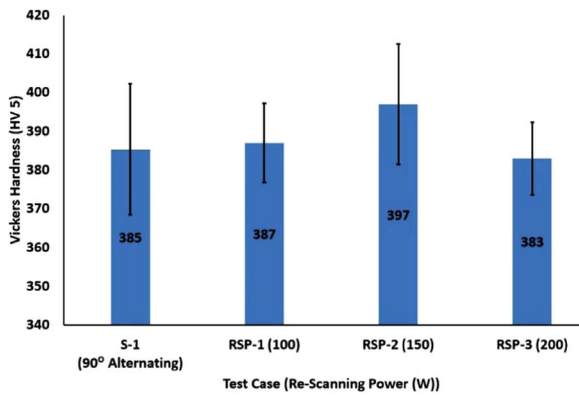


Fig. 26. Effect of re-scanning energy varying power on Vickers Hardness.

elongation compared with test case RSP-1. The amount of porosity decreased as well so therefore the only probable reason for this decrease in elongation for test case RSP-2 samples could be the increase in the oxide layer thickness between Ti6Al4V layers due to re-melting of each layer as Vaithilingam et al. [42] reported formation of oxide layer with re-melting. The elongation of test case

RSP-2 is 5.9% higher than the standard samples of test case S-1, without any rescanning. This could be attributed to the probable transformation of  $\alpha'$  martensite into  $\alpha + \beta$ .

Increasing the rescan power to 200 W, test case RSP-3 resulted in a sharp drop of 53.5% in elongation compared to S-1. Fig. 22(c) shows some micro porosity in test case RSP-3 samples but this alone does not account for such a sharp decline in elongation. Another probable reason for this decrease in elongation for test case RSP-3 samples could be the increase in the oxide layer thickness between Ti6Al4V layers due to re-melting of each layer as Vaithilingam et al. [42] reported formation of oxide layer with re-melting. Increasing the rescanning power to 200 W, test case RSP-3, probably increased the possibility of increase in the oxygen penetration further into the surface as Vaithilingam et al. [42] reported increase in oxygen penetration with re-melting. It is hereby proposed that increase in re-melted melt-pool size has a direct relation with the oxide layer thickness. Thus the melt-pool size comparison from Fig. 18, suggests that rescanning with 100  $\mu$ s exposure would result in thicker oxide layer formation between the layers of the samples. Therefore it is valid to assume that it is these thick oxide layers resulting in the decreased elongation for test case RSP-3.

Fig. 19 showed that increasing rescanning power led to a decrease in cooling rate but the cooling rates are still much higher than  $\frac{100}{s}$ , cooling rate leading totally martensitic microstructure for Ti6Al4V [38]. Since all the test cases RSP-1, RSP-2, and RSP-4 had a totally martensitic microstructure so therefore there is no major variation in Vickers hardness values for samples manufactured with different rescanning powers as shown in Fig. 26.

#### 4. Conclusions

90° alternating scanning strategy resulted in the lowest residual stress build-up for SLM Ti6Al4V parts built on both the standard and modified Renishaw platforms using a modulated Nd-YAG fiber laser. Chessboard scanning showed an increasing trend in residual stress with increasing chessboard block size (scan vector length). Scan vector rotation in adjacent chessboard blocks resulted in a variation in residual stress for the same chessboard block size and therefore there is a possibility of reaching a combination of rotation of scan vectors in adjacent blocks and the whole chessboard for residual stress reduction. Scanning strategy did not show any direct correlation with mechanical properties and neither was a clear dependence of mechanical properties on sample porosity level established.

Re-scanning with varying re-scanning energy density by

maintaining power constant and varying exposure time generally did not yield any promising results in terms of residual stress reduction, this except when re-scanning with 150% energy density which resulted in 33.6% reduction in residual stress. Even though re-scanning with 150% energy density resulted in lower residual stress, the effect on mechanical properties was detrimental and samples failed prematurely possibly due to the thick oxide layer formation due to re-melting.

Re-scanning with varying re-scanning energy density by keeping exposure constant and varying power did not yield any promising results in terms of residual stress reduction and in all cases resulted in higher residual stress than without rescanning case. Rescanning with 50% energy density (100 W power and 100  $\mu$ s exposure) resulted in an increase elongation due to probable transformation of martensitic  $\alpha'$  to  $\alpha + \beta$  microstructure. Even though the %elongation increased with lower power rescanning but the porosity increased to 2.4% due to the rescanning energy being well below the required energy density for complete re-melting of SLM Ti6Al4V. The residual stress also showed an increase of 68.2%.

Therefore based on the results of this study rescanning is not feasible for SLM Ti6Al4V parts, due to the increased build time and the detrimental effect on residual stress build-up and as well as mechanical properties of parts built on the Renishaw SLM platforms.

#### Acknowledgements

The author would like to thank TWI and the EPSRC Future Manufacturing Hub in Manufacture using Advanced Powder Processes (MAPP)(EP/P006566/1) for their support during this investigation.

#### References

- [1] M. Burns, *Automated Fabrication: Improving Productivity in Manufacturing*, Prentice Hall, Englewood Cliffs, NJ, 1993.
- [2] I. Gibson, D.W. Rosen, B. Stucker, *Additive Manufacturing Technologies: rapid Prototyping to Direct Digital Manufacturing*, Springer, 2009, pp. 1–14.
- [3] C. Casavola, S.L. Campanelli, C. Pappalettere, Experimental analysis of residual stresses in the Selective Laser Melting process, in: Proceedings of the XIth International Congress and Exposition, Orlando, Florida, USA, 2008.
- [4] L. Papadakis, A. Loizou, J.R.S.B. A thermo-mechanical modeling reduction approach for calculating shape distortion in SLM manufacturing for aero engine components in VRAP Advanced Research in Virtual and Rapid Prototyping, Portugal.
- [5] J.-P. Kruth, et al., Assessing and comparing influencing factors of residual stresses in selective laser melting using a novel analysis method, Proc. Inst. Mech. Eng., Part B: J. Eng. Manuf. 226 (6) (2012) 980–991.
- [6] J.-P. Kruth, M. Badrossamay, E.Yasa, J. Deckers, L. Thijs, J. Van Humbeeck, Part and material properties in selective laser melting of metals, in: Proceedings of the 16th International Symposium on Electromachining (ISEM XVI), Shanghai, China, 2010.
- [7] M. Matsumoto, et al., Finite element analysis of single layer forming on metallic powder bed in rapid prototyping by selective laser processing, Int. J. Mach. Tools Manuf. 42 (1) (2002) 61–67.
- [8] M.F. Zaeh, G. Branner, Investigations on residual stresses and deformations in selective laser melting, Prod. Eng.: Res. Dev. Ger. 4 (2010) 1.
- [9] P.J. Withers, H.K.D.H. Bhadeshia, Residual stress. Part 1 – measurement techniques, Mater. Sci. Technol. 17 (4) (2001) 355–365.
- [10] P.J. Withers, H.K.D.H. Bhadeshia, Residual stress Part 2- nature and origins, Mater. Sci. Technol. 17 (4) (2001) 366–375.
- [11] L.V. Van Belle, Guillaume Boyer, Jean Claude, Investigation of residual stresses induced during the selective laser melting process, Key Eng. Mater. 554–557 (2013) 1828–1834.
- [12] T.U. Tatsuki Furumoto, Mohd Sanusi Abdul Aziz, Akira Hosokawa, Ryutaro Tanaka, Study on reduction of residual stress induced during rapid tooling process- Influence of heating conditions on residual stress, Key Eng. Mater. 487–488 (2010) 785–789.
- [13] I.A. Roberts, Investigation of Residual Stresses in the Laser Melting of Metal Powders in Additive Layer Manufacturing, University of Wolverhampton, 2012, p. 246.
- [14] S.F. Joe Elambasseril, Matthias Bringezu, Milan Brandt, Influence of process parameters on selective laser melting of Ti 6Al-4V components, RMIT University School of Aerospace, Mechanical and Manufacturing Engineering (SAMME), 2012.
- [15] S. Das, M. Wohlert, J.J. Beaman, D.L. Bourell, Producing metal parts with selective laser sintering/hot isostatic pressing, JOM 50 (12) (1998) 17–20.
- [16] F. Verhaeghe, et al., A pragmatic model for selective laser melting with evaporation, Acta Mater. 57 (20) (2009) 6006–6012.
- [17] S.A. Khairallah, A. Anderson, Mesoscopic simulation model of selective laser

- melting of stainless steel powder, *J. Mater. Process. Technol.* 214 (11) (2014) 2627–2636.
- [18] Y. Lu, et al., Study on the microstructure, mechanical property and residual stress of SLM Inconel-718 alloy manufactured by differing island scanning strategy, *Opt. Laser Technol.* 75 (2015) 197–206.
- [19] A.J. Dunbar, et al., Development of experimental method for in situ distortion and temperature measurements during the laser powder bed fusion additive manufacturing process, *Addit. Manuf.* (12, Part A) (2016) 25–30.
- [20] A.H. Nickel, D.M. Barnett, F.B. Prinz, Thermal stresses and deposition patterns in layered manufacturing, *Mater. Sci. Eng.: A* 317 (1–2) (2001) 59–64.
- [21] A.V. Gusarov, M. Pavlov, I. Smurov, Residual stresses at laser surface remelting and additive manufacturing, *Phys. Procedia* 12 (2011) 248–254.
- [22] B. Cheng, S. Shrestha, K. Chou, Stress and deformation evaluations of scanning strategy effect in selective laser melting, *Addit. Manuf.* (12, Part B) (2016) 240–251.
- [23] S. Safdar, et al., An anisotropic enhanced thermal conductivity approach for modelling laser melt pools for Ni-base super alloys, *Appl. Math. Model.* 37 (3) (2013) 1187–1195.
- [24] A. Vasinonta, J.L. Beuth, M. Griffith, Process maps for predicting residual stress and melt pool size in the laser-based fabrication of thin-walled structures, *J. Manuf. Sci. Eng.* 129 (1) (2006) 101–109.
- [25] I. Van Zyl, I. Yadroitsev, I. Yadroitsava, Residual stresses in direct metal laser sintered parts, 2015.
- [26] L. Parry, I.A. Ashcroft, R.D. Wildman, Understanding the effect of laser scan strategy on residual stress in selective laser melting through thermo-mechanical simulation, *Addit. Manuf.* (12, Part A) (2016) 1–15.
- [27] H. Pohl, et al. Thermal stresses in direct metal laser sintering, in: *Proceedings of the 12th Solid Freeform Fabrication Symposium*, Austin, TX, 2001.
- [28] A.S. Wu, et al., An experimental investigation into additive manufacturing-induced residual stresses in 316L stainless steel, *Metall. Mater. Trans. A* 45 (13) (2014) 6260–6270.
- [29] P. Mercelis, J.-P. Kruth, Residual stresses in selective laser sintering and selective laser melting, *Rapid Prototyp. J.* 12 (5) (2006) 254–265.
- [30] M. Shiomi, et al., Residual stress within metallic model made by selective laser melting process, *CIRP Ann. Manuf. Technol.* 53 (1) (2004) 195–198.
- [31] ASTM, E2109-01(2007), Standard Test Methods for Determining Area Percentage Porosity in Thermal Sprayed Coatings, ASTM International, West Conshohocken, PA, 2007.
- [32] BSI, BS 7590:1992, Method for statistically estimating the volume fraction of phases and constituents by systematic manual point counting with a grid, BSI, 1992.
- [33] ASTM, E8 / E8M-13a, Standard Test Methods for Tension Testing of Metallic Materials, ASTM International: West Conshohocken, PA, 2013.
- [34] BSEN, ISO 6892-1, Metallic materials. Tensile testing. Method of test at ambient temperature, 31 August, 2009.
- [35] BSEN, ISO 6507-1:2005, Metallic materials. Vickers hardness test. Test method, 2006.
- [36] A. Simchi, Direct laser sintering of metal powders: mechanism, kinetics and microstructural features, *Mater. Sci. Eng.: A* 428 (1) (2006) 148–158.
- [37] H. Ali, et al., In-situ residual stress reduction, martensitic decomposition and mechanical properties enhancement through high temperature powder bed pre-heating of selective laser melted Ti6Al4V, *Mater. Sci. Eng.: A* 695 (2017) 211–220.
- [38] T. Ahmed, H.J. Rack, Phase transformations during cooling in  $\alpha + \beta$  titanium alloys, *Mater. Sci. Eng.: A* 243 (1–2) (1998) 206–211.
- [39] E. Yasa, J.P. Kruth, Microstructural investigation of Selective Laser Melting 316L stainless steel parts exposed to Laser re-Melting, *Procedia Eng.* 19 (2011) 389–395.
- [40] G. Kasperovich, J. Hausmann, Improvement of fatigue resistance and ductility of TiAl6V4 processed by selective laser melting, *J. Mater. Process. Technol.* 220 (2015) 202–214.
- [41] P. Mercelis, Control of Selective Laser Sintering and Selective Laser Melting Processes, KU Leuven, Leuven, Belgium, 2007.
- [42] J. Vaithilingam, et al., The effect of laser remelting on the surface chemistry of Ti6Al4V components fabricated by selective laser melting, *J. Mater. Process. Technol.* 232 (2016) 1–8.
- [43] S. Leuders, et al., On the mechanical behaviour of titanium alloy TiAl6V4 manufactured by selective laser melting: fatigue resistance and crack growth performance, *Int. J. Fatigue* 48 (2013) 300–307.
- [44] M. Simonelli, Y.Y. Tse, C. Tuck, The formation of  $\alpha + \beta$  microstructure in as-fabricated selective laser melting of Ti–6Al–4V, *J. Mater. Res.* 29 (17) (2014) 2028–2035.